SBF
SOCIEDADE BRASILEIRA DE FÍSICA
CrossMark

CONDENSED MATTER

# Physical Property Characterization of Pb²⁺-Doped CdS Nanofilms Deposited by Chemical-Bath Deposition at Low Temperature

**J. Díaz-Reyes** [1] · **J. I. Contreras-Rascón** [2] · **M. Galván-Arellano** [3] · **J. S. Arias-Cerón** [4] · **J. E. M. Gutiérrez-Arias** [5] · **J. E. Flores-Mena** [5] · **M. M. Morín-Castillo** [5]

**Abstract** Pb²⁺-doped CdS nanofilms are prepared using the growth technique chemical bath deposition (CBD) under optimum conditions lead acetate at the reservoir temperature of $20 \pm 2$ °C. The Pb²⁺ molar concentration was in the range $0.0 \leq x \leq 0.19.67$, which was determined by energy-dispersive X-ray spectroscopy (EDS). The X-ray diffraction results show that the films are of PbS–CdS composites with individual CdS and PbS planes. The X-ray diffraction (XRD) analysis and Raman scattering reveal that CdS-deposited films showed the zincblende (ZB) crystalline phase. The average grain size of the CdS films ranged from 1.21 to 6.67 nm that was determined by the Debye–Scherrer equation from ZB (111) direction, and it was confirmed by high-resolution transmission electron microscopy (HRTEM). Raman scattering shows that the lattice dynamics is characteristic of bimodal behaviour and the multipeaks adjust of the first optical longitudinal mode for the Pb²⁺-doped CdS denotes the Raman shift of the characteristic peak in the range of 305–298 cm⁻¹ of the CdS crystals, which is associated with the lead ion incorporation. The films exhibit three direct bandgaps, ~2.44 eV attributed to CdS; the other varies continuously from 1.67 to 1.99 eV and another disappears as Pb²⁺ molar fraction increases.

## 1 Introduction

The development of third-generation solar cells overcoming the Shockley–Queisser efficiency limit for a single absorber, 31 %, is one of the most fascinating challenges in the energy research field. In this aspect, semiconductor quantum dots (QDs) have shown extremely attractive properties for the development of solar cells overcoming the current limitations. The demonstration of an efficient multiple exciton generation (MEG) process in colloidal QDs, despite certain controversy, has aroused a huge interest in the use of these materials in photovoltaic devices. This interest has been reinforced with the recent reports of absorbed photon-to-current efficiency (APCE) close to 200 % and incident photon-to-current efficiency (IPCE) as high as 114 %. In the former case, PbS QDs have been employed in a sensitized solar cell configuration. An attempt was made to modify the bandgap of CdS (~2.4 eV) by preparing a mixed lattice with a low-bandgap material, PbS (0.3 eV), giving a new set of materials, $Cd_{1-x}Pb_xS$. Bandgaps, as low as ~1.9 eV, were achieved with increasing $x$. The ternary semiconductor $CdS_{1-x}Pb_x$ is characterized by having a wide bandgap at room temperature of 0.37 eV PbS to 2.4 eV of CdS. It is a

✉ J. Díaz-Reyes
joel_diaz_reyes@hotmail.com

1  Centro de Investigación en Biotecnología Aplicada, Instituto Politécnico Nacional, Ex-Hacienda de San Juan Molino, Km. 1.5., 90700 Tepetitla, Tlaxcala, Mexico

2  División de Ciencias Exactas y Naturales, Departamento de Física, Universidad de Sonora, Col. Centro, 83000 Hermosillo, Sonora, Mexico

3  Depto. de Ingeniería Eléctrica, SEES, CINVESTAV-IPN, Apartado Postal 14-740, 07000 Mexico, D. F., Mexico

4  Catedrático CONACYT, Depto. de Ingeniería Eléctrica, SEES, CINVESTAV-IPN, Apartado Postal 14-740, 07000 Mexico, D.F., Mexico

5  Facultad de Ciencias de la Electrónica, Benemérita Universidad Autónoma de Puebla, Av. San Claudio y 18 Sur. Col. San Manuel, Ciudad Universitaria Puebla, 72570 Puebla, Mexico

semiconductor with multiple applications in the technology field for its unique properties of detection, such as infrared detectors, photoresists solar cells for their ecological aspect and the effect of multiple exciton generation was recently discovered in PbS nanostructures, which is promising for such applications, for use in electronic applications thin films transistors (TFTs). Photosensitivity of detectors can be improved by adjusting the gate voltage and in the manufacture of laser diodes by its corresponding emission spectral range 2.7–4.2 μm [1]. Today, it is accepted that the thin films of lead sulphide deposited by chemical bath are p-type due to oxidation processes taking place during deposition.

This work reports the growth and characterization of CdS:$Pb^{2+}$ nanofilms obtained by chemical bath deposition on glass substrate at low temperature. The effects of the chemical composition on structural and optical properties of the CdS:$Pb^{2+}$ alloy were studied by X-ray diffraction, HRTEM, EDS, Raman scattering and transmittance.

## 2 Experimental Details

The chemical bath is a technique to deposit and grow films on a solid substrate from a reaction that occurs in solution. It starts from an aqueous solution of salts of the elements of the compound to be obtained. It is required that the compound to deposit is relatively insoluble and chemically stable in the solution to give a simple precipitation in an ionic reaction [2, 3]. For the synthesis of CdS:$Pb^{2+}$, the metal ion source is lead acetate, the hydroxyl ion source is sodium hydroxide, and the sulphur source is thiourea ions and complexing agent, ammonium nitrate [4]. All used chemical reagents were from Sigma-Aldrich except for cadmium sulphate which was from Merck Millipore. The feasibility of this technique for its environment is a deposit short time, it does not require high temperatures, there is no emission of toxic gases into the atmosphere and the preparation of the solutions is carried out micro scale. For carrying out the intentional doping by lead of the deposited layers, small lead acetate volumes are added to the growth solution in the range of 0 to 30 ml to obtain different lead concentrations in the nanostructures, which are presented in Table 1. The CdS:$Pb^{2+}$ nanofilm chemical stoichiometry and surface morphology were obtained by scanning electron microscopy and energy-dispersive spectrometry (SEM–EDS), which were carried out in a System LEO 438VP, with W.D. of 26 mm using a pressure of 20 Pa. The crystalline phase and structure of the films were determined with a Bruker D8 Discover diffractometer using copper Kα radiation ($\lambda$ = 1.5406 Å) at 40 kV and 40 mA with parallel beam geometry. High-resolution transmission electron

microscopy (HRTEM) studies were carried out in a JEOL JEM200 of 80–200 KV; the obtained image is recorded with a CCD camera in real time. The Gatan Digital Micrograph software was used for the analysis of HRTEM images. Raman scattering experiments were performed at room temperature using the 6328 Å line of a He–Ne laser at normal incidence for excitation. The light was focused to a diameter of 6 μm at the sample using a ×50 (numerical aperture 0.9) microscope objective. The nominal laser power used in these measurements was 20 mW. Care was taken to avoid the heating of the sample inadvertently to the point of changing its Raman spectrum. Scattered light was analysed using a Dilor micro-Raman system (Lambram model), a holographic notch filter made by Kaiser Optical System, Inc. (model superNotch-Plus), a 256 × 1024-pixel CCD used as detector cooled to 140 K using liquid nitrogen and two interchangeable gratings (600 and 1800 g/mm). Typical Raman spectrum acquisition time was limited to 60 s to minimize the sample heating effects discussed above. Absolute spectral feature position calibration to better than 0.5 cm$^{-1}$ was performed using the observed position of Si which is shifted by 521.2 cm$^{-1}$ from the excitation line [5]. The transmittance measurement was performed using a Bruker Infrared Spectrometer Vertex 70 at room temperature.
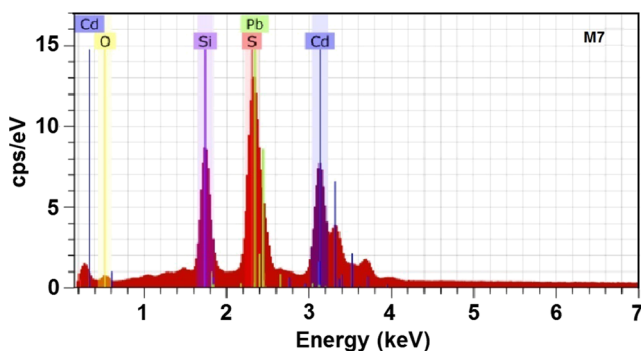
## 3 Results and Discussion

The chemical composition of the CdS:$Pb^{2+}$ films was estimated by EDS measurements, which besides allow knowing the presence of some residual impurities. Figure 1 shows the EDS spectrum of one typical sample, M7, which indicates the presence of oxygen in the samples along with cadmium, sulphur and lead. The EDS spectra indicate that besides the samples contain a significant amount of silicon, potassium, calcium, sodium and oxygen, and other residual impurities. Thus, most of the residual impurities detected in the layers come from the substrate, which is Corning glass. By XPS analysis, in other materials as ZnS, it has been showed that oxygen ions are present in the samples in the form of $O^{2-}$ ions that may produce CdO in the samples [6]. Oxidation of CdS to CdO occurs at high temperatures as has been reported by many researcher groups [7]. Since the temperature during synthesis and air-drying in the present case is low, this conversion may have happened only at a very low percentage so that the presence of CdO could not be detected in X-ray diffraction measurements. However, these oxygen ions can form trap levels in the bandgap, resulting in several transitions contributing to luminescence. Thus, it appears that oxygen has replaced sulphur at some random points of the CdS:$Pb^{2+}$ lattice. The results of such measurements are shown in Table 1,

**Table 1** Summary of the CdS:Pb$^{2+}$ samples grown and studied in this work and the doping volume added to each one. The Pb, Cd and S concentrations in as-deposited samples were estimated by means of energy-dispersive spectroscopy (EDS). The average errors that were calculated percentage masses of different elements were for cadmium 1.25 %, sulphur 0.35 % and lead 0.25 %. For a stoichiometric compound (CdS), the percentage atomic masses are cadmium 77.81 % and sulphur 22.19 %

| Sample | Pb(C$_2$H$_3$O$_2$)$_2$ added volume (ml) | Cd mass weight (%) | Cd molar fraction (%) | S mass fraction (%) | S molar fraction (%) | Pb mass fraction (%) | Pb molar fraction (%) |
|--------|-------------------------------------------|--------------------|----------------------|---------------------|----------------------|----------------------|-----------------------|
| M1 | 00 | 82.01 | 56.53 | 17.99 | 43.47 | 0.00 | 0.00 |
| M2 | 05 | 74.06 | 52.33 | 18.26 | 44.21 | 7.68 | 3.45 |
| M3 | 10 | 73.03 | 51.69 | 15.79 | 42.74 | 11.18 | 5.58 |
| M4 | 15 | 61.19 | 48.29 | 12.71 | 38.10 | 26.10 | 13.61 |
| M5 | 20 | 58.68 | 47.12 | 11.38 | 38.14 | 29.94 | 14.70 |
| M6 | 25 | 56.90 | 45.83 | 11.27 | 38.46 | 31.83 | 18.72 |
| M7 | 30 | 56.47 | 41.16 | 11.23 | 39.17 | 32.81 | 19.67 |

in which is included the atomic and mass percentages. From these results is observed that sample M1, CdS, is not a stoichiometric compound and that starting from it a higher thiourea concentration in the solution gives a higher presence of cadmium and lead in the material and an absence of sulphur. Continuing with the consideration that each unit cell of CdS contains two cadmium atoms and two sulphur atoms, the atomic weight of the ideal unit cell is ~288.95 corresponding to 22.19 % sulphur atoms and 77.81 % cadmium atoms. Then, when a stoichiometric deviation of the ideal unit cell occurs, it could establish a correspondence between vacancies or interstices of some of the compound elements (V$_S$, V$_{Cd}$, Cd$_i$, S$_i$). In the case of M1, it has an excess of Cd and absence of sulphur, which is indicative that cadmium is interstitial and there are vacancies of sulphur. The average errors with which were calculated percentage masses of different elements were for cadmium 1.25 %, sulphur 0.35 % and lead 0.25 %. As you can see in Table 1, these errors do not significantly alter the above findings. Table 1 shows that the samples contain a lower concentration of sulphur, indicating that they have a high concentration of sulphur vacancies. Also, it can induce that there is a high concentration of cadmium and lead interstices. Therefore, in the samples studied in this work

there is excess of II and IV elements and of VI element deficiency in the range of investigated lead concentration.

Figure 2 shows X-ray patterns of CdS:Pb$^{2+}$ nanofilms with different lead concentrations deposited at a temperature of 20 ± 2 °C. It is observed from the XRD patterns that CdS:Pb$^{2+}$ films deposited are in polycrystalline nature. It can be seen that each peak corresponds fairly well with data of CdS:Pb$^{2+}$ marked in the software DICVOL04 data. The obtained structural parameters with the software DICVOL04 data are in good agreement with the published ones. From this close agreement, it is confirmed that as-deposited CdS:Pb$^{2+}$ nanofilms for all the thiourea concentrations belong to the cubic crystal system. The X-ray patterns of deposited CdS:Pb$^{2+}$ thin films are described in the *Fm-3m(225)* and whose lattice parameters were calculated using the software DICVOL04, obtaining the following lattice parameters values: $a$ = 5.73 Å, which are in agreement with the reported values [8, 9]. CdS exists in two crystalline modifications: the
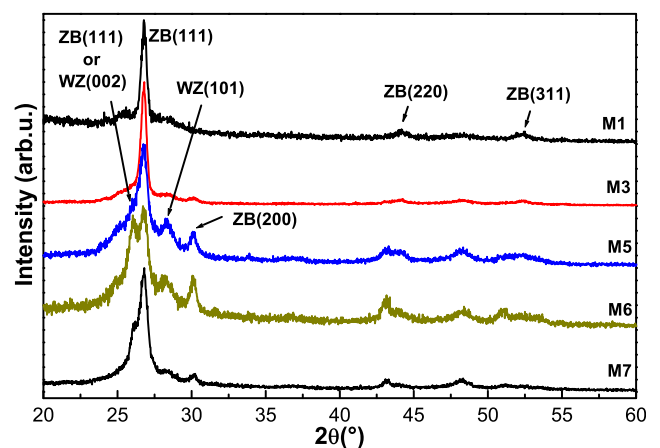


**Fig. 1** EDS spectrum of one Pb-doped CdS typical sample, M7. The spectrum indicates that besides Cd, Pb and S, the samples contain a significant amount of residual impurities that come from the substrate



**Fig. 2** XRD diffraction patterns for CdS and CdS:Pb films. M1 diffractograms display peaks at $2\theta$ = 26.81°, 44.16° and 52.44°. They are related to the (111), (220) and (311) reflection planes for the ZB phase of the CdS, respectively. All the diffraction peaks can be perfectly matched to the reference patterns (JDDC 0531447) displaying the ZB crystalline phase

wurtzite (WZ) [10] and zinc blende (ZB) phase [9]. As can be seen, the obtained diffraction pattern for sample M1 shows a predominant peak at $2\theta = 26.81°$, which can be assigned to (111) plane of ZB CdS phase. Moreover, the intensity weak of peak at $2\theta = 28.27°$ is due to diffraction from the (101) plane WZ phase whereas at $2\theta = 26.44°$ position can be co-occupied by the (111) plane of ZB phase as well as the (002) plane WZ. However, the maximum peak intensity for both crystalline phases is different; ZB maximizes at $2\theta = 26.81°$ corresponding to the (111) plane, whereas WZ phase has its maximum intensity peak at $2\theta = 28.20°$ corresponding to (101) plane [11]. Formation of the WZ phase is likely, at least to large extent, because the characteristic diffraction peak from the (002) planes of the structure was completely absent when the CdS film was deposited. The shift in the diffraction angles is due to the incorporation of $Pb^{2+}$ at the sub-lattice sites of $Cd^{2+}$. It has been reported in the literature that the probability that CdS dissolves in the PbS lattice at room temperature is very low [12]. In this case of extremely small particles, where the contribution of surface free energy is very important, some deviations cannot be excluded. From XRD patterns, it can be assured that the $Pb^{2+}$ forms PbS according to the peak observed at $2\theta \sim 30.01°$ in M5 and M6 samples.

From the XRD study, it can be inferred that the formation of the CdS:$Pb^{2+}$ occurs in the early stage, following by the formation of PbS nanocrystallites in the stage of the film growth, although the formation of films from the bath in absence of acetic is also observed [13]. It is found in this study that the reaction leads to formation of nanocrystalline CdS:PbS films together with a slight decrease in the size of crystallites. Besides, a widening at the peak of the preferential (111) direction is observed, which could be caused by undergoing stress, the size of the small crystalline domain or fluctuations in concentration. The first case does not happen since the used substrate is amorphous and it does not produce a mismatch in the material lattice parameters. The variation in the size of the average crystalline domain is the cause of this widening that can be due to the small size of the crystals and by presence of strains that possess multiple facet diffraction peaks, which is the result of multidirectional growth of the synthetized nanocrystals. In fact, to apply the Debye–Scherrer equation [14], one finds that the crystalline domain increases. The mean grain size was calculated from cubic (111) reflection of CdS:$Pb^{2+}$ for all the studied samples. It is worth noting the values of electronegativity for Pb (2.33) and Cd (1.69), which are favourable to form a solid solution [15]. These results show that the grain size increases as the thiourea concentration is increased in the growth solution as can be observed in Table 1 and Fig. 2.

Figure 3 shows the variation of the size of the average crystalline domain with the lead incorporation obtained by the Debye–Scherer equation through the measurement of the width at half maximum (FWHM) of the more intense
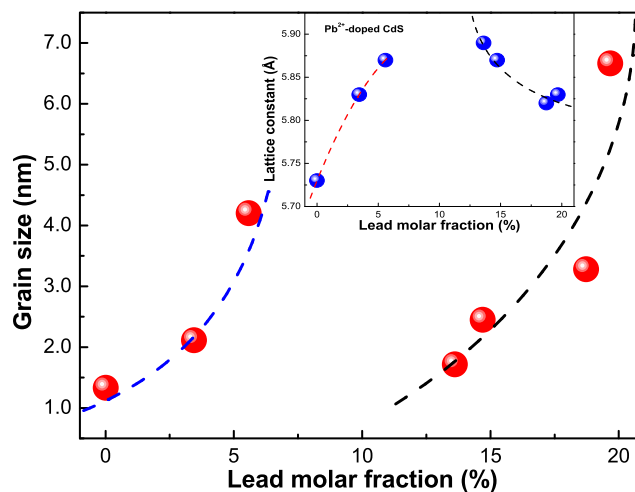


Fig. 3 Dependence of the grain size of the average crystalline domain based on the increase of lead molar fraction for the CdS:$Pb^{2+}$ system. The *inset* shows lattice constant as function of Pb molar fraction

peak that is (111) direction of deposited layers, which is sited about 26.81°. The intensity of this peak depends lightly of the lead molar fraction in the nanofilms. The dash lines are some figures of merit for following the behaviour of experimental points, as is observed there are regions, the first one corresponds at low lead concentrations, M1, M2 and M3 samples, and the second one to high lead concentrations, where clearly is observed the $Pb^{2+}$ effect to replace Cd ions of the CdS:$Pb^{2+}$ lattice. Similar behaviour is observed for the lattice constant, as shown in the inset of Fig. 3. For the interplanar distance (ID) (111) for the ZB phase presented in Table 2, calculated from the $2\theta$ peak position, versus lead molar fraction, increases lightly. This ID, in practice, coincides with (111) ID of the ZB phase.

It can be seen that it increases as V[$Pb^{2+}$] increases, suggesting the formation of a solid solution and then it goes up again, having a region of discontinuity, for higher V[$Pb^{2+}$]. This is consistent with a single phase material at lowest V[$Pb^{2+}$] and a two-phase material at higher V[$Pb^{2+}$]. Moreover, the lattice constant increases with increasing V[$Pb^{2+}$] in the film which is an effect of $Pb^{2+}$ substituting $Cd^{2+}$ in CdS. A possible explication to this experimental fact can be due to the difference of the ionic radii of $Cd^{2+}$ (0.97 Å) and $Pb^{2+}$ (1.20 Å). The (111) ID of ZB phase in bulk are 3.367 Å. These values are larger than the ID values found for the CdS–CdSPb films in this work. It is probable that values of ID in CdS:$Pb^{2+}$ nanofilms are owing to the existence of $Cd^{2+}$ vacancies. For a relative low concentration of the $Pb^{2+}$ ion, this can be, in a large majority, situated in (a) $Cd^{2+}$ vacancies sites which otherwise would be empty [16], (b) $Cd^{2+}$ sites provoking the appearing of $Cd^{2+}$ interstitial and (c) interstitial positions. For higher V[$Pb^{2+}$], the material behaves like a

**Table 2** The mean grain sizes of the nanofilms obtained by the Debye–Scherrer equation for the direction ZB (111), which show the dependence of the grain size of the average crystalline domain based on the increase of Pb molar fraction for the CdS:Pb$^{2+}$ system. Besides, it presents the grain sizes obtained by TEM. Additionally, the interplanar distance and optical bandgap energies obtained by transmittance measurements are shown

| Sample | $a_{X\text{-ray}}$ (Å) | $d_{(111)}$ (nm) | Grain size (X-ray) (nm) | Grain size (TEM) (nm) | Bandgap I (eV) | Bandgap II (eV) | Bandgap III (eV) |
|--------|------------|----------|-----------|-----------|-----------|-----------|-----------|
| M1 | 5.73 | 0.28 | 2.12 | 5.11 | 2.49 | 1.67 | 0.98 |
| M2 | 5.83 | 0.29 | 1.33 | – | 2.45 | 1.97 | 2.09 |
| M3 | 5.87 | 0.29 | 1.21 | 5.50 | 2.44 | 1.96 | 2.06 |
| M4 | 5.89 | 0.31 | 1.72 | – | 2.49 | 1.99 | 2.01 |
| M5 | 5.87 | 0.33 | 2.45 | 5.85 | 2.46 | 1.84 | |
| M6 | 5.84 | 0.33 | 3.28 | 3.50 | 2.34 | 1.77 | |
| M7 | 5.83 | 0.33 | 6.67 | – | 2.27 | 1.71 | |

solid solution; the generation of Cd$^{2+}$ vacancies, whose creation is needed to charge balance, starts to be important in number and given the relative ionic radius of S$^{2-}$. There is a tendency of the full width at half maximum (FWHM) of (111) peak [17] of the grown films probably due to all of the possible Pb$^{2+}$ species present in Cd$^{2+}$ sites and interstitial positions, and also to the existence of PbS, which distort the crystalline lattice and provoke structural disorder. The distortion produces a strong strain which affects the interatomic distances; this similar fact has already been reported [18]. In this work, the strain and distortion of the lattice can be smaller. The appearing of S$^{2-}$ ions into the material favours the relaxing of the lattice. Figure 4 illustrates images obtained by high-resolution transmission electron microscopy for some typical samples, and the insets are the result of the processing of the HRTEM image using filters in Fourier space. As is observed in figures, there are two structure types; at low V[Pb$^{2+}$], the crystal nanostructures are nearly spherical in shape of the material with an average size of ~1.33–6.67 nm, and to the sample with higher V[Pb$^{2+}$], they contain nanostructures with a box shape, whose dimensions are approximately (11.30–12.82) nm × (6.32–8.72) nm (see Fig. 4d). This behaviour has been observed in other materials, which by changing the concentrations of the precursors or the experimental conditions the nanoparticles' shape changes. The most direct way of controlling the reaction kinetics, and thus particle shape, in these syntheses is by changing the concentration of the lead reducing agent. Increasing the amount of lead in the growth solution increases the rate of lead ion reduction, which should create a preference for the growth of more kinetically favourable (or less thermodynamically favourable) particle morphologies [19, 20]. Furthermore, in the insets can clearly observe the interplanar distance between two adjacent parallel planes of atoms, which correspond to the direction of the cubic phase of CdS:Pb$^{2+}$ (111). As can be seen, the results obtained by HRTEM are

in good agreement with the results calculated from X-ray diffraction using the Debye–Scherrer equation.

It is well known that vibrational spectroscopy is a very useful technique for the determination of the crystal phase. Furthermore, Raman spectroscopy of semiconductors is a fast and non-destructive tool to appreciate crystalline material qualities, including surface conditions and homogeneity. That is, crystalline samples present sharp Raman peaks while amorphous or polycrystalline samples show very broad Raman peaks [21]. So, the structural characterization of the as-synthesized CdS nanostructures was therefore carried out using Raman spectroscopy. Each of the phonon wavenumbers was extracted by fitting the Raman spectrum to a Lorentz line shape, and the first longitudinal optical (1LO) and second longitudinal optical (2LO) phonons and multiphonon processes can be clearly observed in Fig. 5, which correspond to a zincblende (ZB) crystalline phase. For a better analysis, the Raman spectra will be divided into two frequency ranges. The first region for frequencies below 200 cm$^{-1}$ and the second one to higher frequencies as are illustrated in Figs. 6a, b, in which Raman spectra of three typical samples, M1, M2 and M7, are displayed. Figure 6a illustrates the CdS:Pb$^{2+}$ Raman spectra in the range from 50 to 200 cm$^{-1}$ for the three typical samples, M1, M2 and M7, showing three vibrational bands, which depend strongly on the lead molar fraction. Besides, it is observed that these bands happened a blue shift as lead concentration is increased. Similar vibration modes were obtained by Raman theories and are in agreement with the results reported by de Wijs et al. [22]. They are the typical characteristic peaks of the zincblende phase at low frequencies that were obtained by deconvolution using Lorentzian curves for finding the peaks' frequency that are associated to lattice modes [23, 24]. As is observed in Figs. 5 and 6a, from M4–M7 Raman spectra the peak about 143 cm$^{-1}$ is well resolved and can be associated to the combination of longitudinal and transverse acoustic phonon modes in PbS

**Fig. 4** HRTEM micrographs of the typical CdS:Pb$^{2+}$ samples: **a** M3, **b** M5, **c** M6 and **d** M7
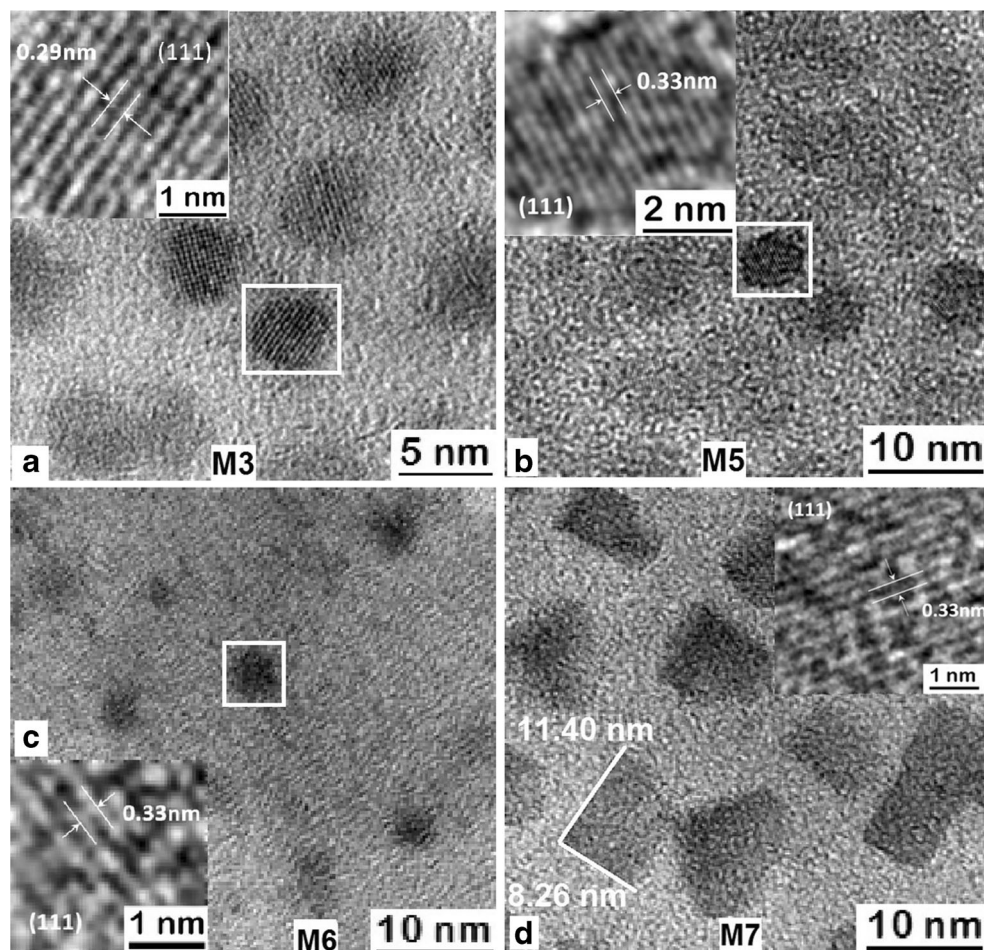


nanocrystals [25]. Then, the second frequency region will be discussed. The Raman peaks of M1 (nanoparticles) appear at 305.1 cm$^{-1}$, attributed to the A$_1$(LO) mode with a full width at half maximum (FWHM) of ca. 24.3 cm$^{-1}$ and its overtone at 600.2 cm$^{-1}$. The Raman peaks of M2 (nanoparticles) appear at 301.2 cm$^{-1}$ with a FWHM of ca. 28.3 cm$^{-1}$ and its overtone at 597.1 cm$^{-1}$. The Raman peaks of M7 (nanoparticles) appear at 298.3 cm$^{-1}$ with a FWHM of ca. 28.1 cm$^{-1}$ and its overtone at 591.4 cm$^{-1}$ [26–28]. As is observed of these results, Raman peaks are red shifted as lead concentration is increased in the nanofilms and the Raman spectra exhibit relatively sharp crystal-like peaks. The light increase of the FWHM from M1 to M2 and M7 can be attributed to a slight deterioration of the crystallinity of the CdS nanocrystals due to the incorporation of lead to Cd sub-lattice. It has been reported that defect-free crystalline CdS films have a FWHM of 8 cm$^{-1}$ [29]. Therefore, grown samples have a high density of structural defects, as had been deduced from the results of the chemical composition. We all know that in a crystalline semiconductor or insulator the observed Raman shifts usually correspond to the LOs, whereas other modes such as the transverse optical and surface

phonon modes are not observable because of symmetry restrictions and their low intensities [30]. Another observation is that the peak profile of the nanoparticles is almost symmetric for the three samples. It is also observed that the intensity of the Raman line LO of sample M2 is lower than that of M1, which is attributed to the quantity of the sample detected by Raman (see Fig. 5). It is known that the intensity of a Raman line is proportional to the number of scattering centres because of the fact that Raman scattering is an incoherent process [31]; in this case, as can be seen in Fig. 6a, the lattice vibrational frequencies are dominant and shielding to the longitudinal optical vibrations, as the V[Pb$^{2+}$] increases. In addition to the LO phonon and its replicas, and lattice vibrations, for sample M1, several peaks are resolved as 263.1, 351.4 and 567.9 cm$^{-1}$ suggesting that the samples have better crystalline quality [32]. The peaks at approximately 263.1, 351.4 and 567.9 cm$^{-1}$ can be assigned to multiphonon scattering, which is consistent with other reports [33]. The feature at the high-energy shoulder, sited at 351.4 cm$^{-1}$, is the subject of a recent study by Dzhagan et al. [34], who suggest that it results from the participation of acoustic phonons to the scattering process and the
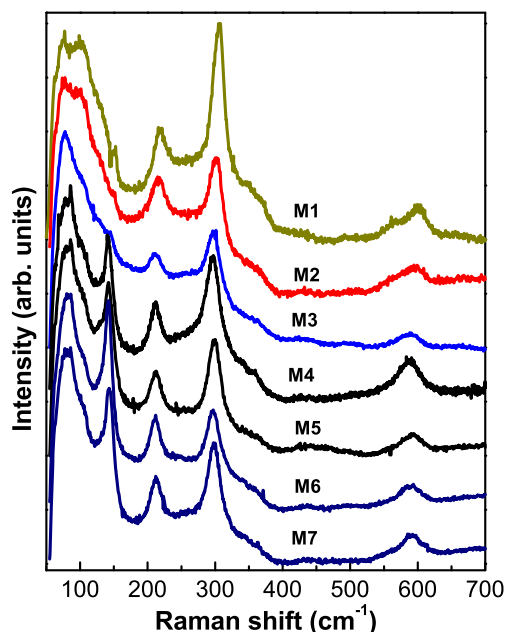
**Fig. 5** Raman spectra of the CdS:Pb$^{2+}$ films added with different lead concentrations

mode corresponding to the low-energy shoulder originates from surface optical phonon modes (SO) at 263.1 cm$^{-1}$ [35, 36]. As is observed in Fig. 6, the frequencies of the vibrational bands decrease as the lead molar fraction increases; this is consistent because the ionic radius of lead is higher than that of cadmium.

The effect of such heavy Pb doping on the optical behaviour of the CdS nanofilms was investigated by measuring its transmission optical absorption. The transmittance spectra in the visible and infrared ranges are recorded for the CdS:Pb$^{2+}$ thin films in the wavelength range 400–2600 nm that were

measured at room temperature, which are illustrated in Fig. 7. The effect of V[Pb$^{2+}$] added in the nanolayers on the optical properties including percentage of transmittance (% of T) and fundamental bandgap energy ($E_g$) were studied in detail. The observed transmittance of the CdS film in the visible range varies from about zero up to nearly 86.5 % (without considering the substrate contribution) and it is higher of all shown transmittance spectra. The sharp reduction in the transmittance spectra at the wavelengths lower than 500 nm is due to the fundamental absorption edges of the different films. The CdS:Pb$^{2+}$ nanofilms were transparent, with no observable blue colouration under our experimental conditions.

The intrinsic absorption edge of the nanofilms can be evaluated and discussed in terms of the indirect interband transition. The optical bandgap ($E_g$) of a semiconductor is related to the optical absorption coefficient ($\alpha$) and the incident photon energy ($h\nu$). The absorption coefficient $\alpha$ for a film of thickness $d$ and reflectance $R$ is determined near the absorption edge using the simple relation: $\alpha = \ln\{(1 - R)^2/T + [((1 - R^2)/2T)^2 + R^2]^{1/2}\}/d$, where multiple reflections are taken into, but interference neglected. Actually, a transmission interference pattern could be observed in most samples, and it was used to obtain an accurate value for the thickness $d$. The optical bandgap of CdS:Pb$^{2+}$ has been evaluated from the transmittance spectrum using the Tauc relation [17, 37–39]: $\alpha h\nu = (E_G - h\nu)^n$, where $n$ depends on the kind of optical transition that prevails. Specifically, $n$ is 1/2 and 2 when the transition is directly and indirectly allowed, respectively. The CdS:Pb$^{2+}$ film is known to be a semiconductor with a directly allowed transition. The CdS:Pb$^{2+}$ optical bandgap energies are evaluated from the absorption coefficient ($\alpha$) using the standard relation: $(\alpha h\nu)^2 = A(h\nu - E_g)$, which is expected to show a linear behaviour in the higher-energy region, which should

**Fig. 6** Decomposition of the measured Raman spectra into individual components for two Raman shift ranges: **a** lower one and **b** higher one. The *dashed lines* are their respective fitting
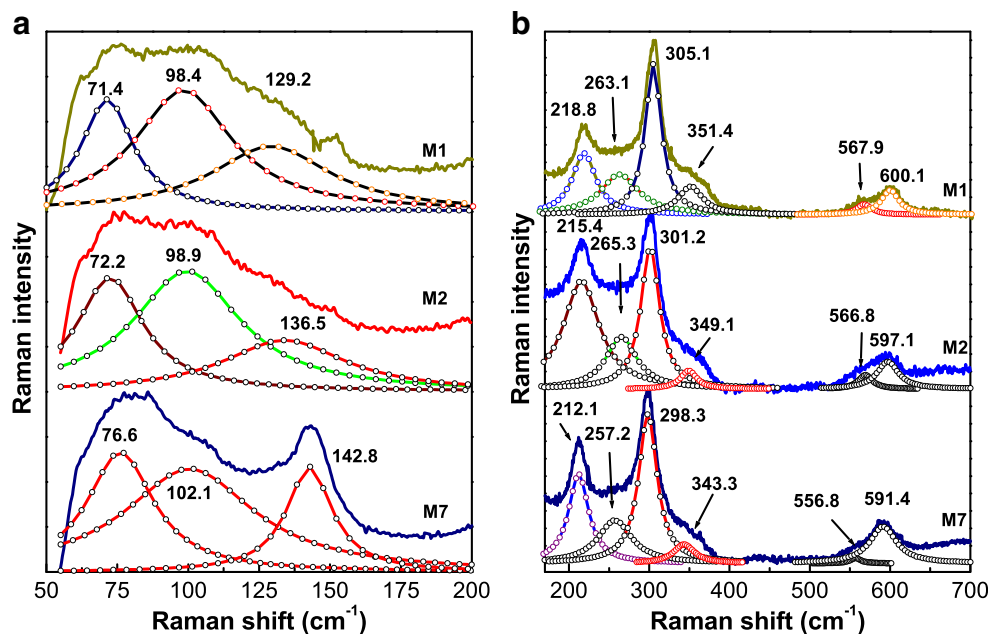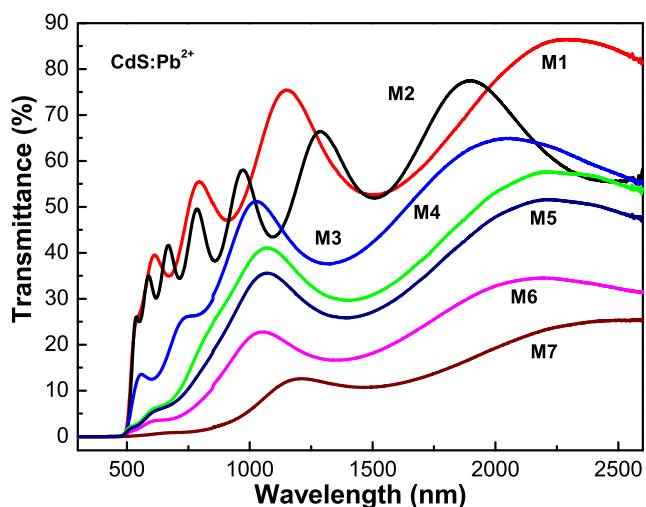
Fig. 7 The transmittance spectra of CdS nanofilms for different $V[Pb^{2+}]$

correspond to a strong absorption near the absorption edge. Extrapolating the linear portion of this straight line to zero absorption edge gives the optical bandgap energy ($E_g$) of the films, which is shown in Fig. 8 for two typical samples (M1 and M7). The obtained results are presented in Table 2. The bandgap value to the sample M1 ($x = 0$) was slightly higher than the value of bulk zincblende CdS (2.4–2.45 eV) [40] due to quantum confinement of CdS nanocrystals. The result reveals that the CdS spectrum exhibits three direct absorption regions, indicated by linear relationships between $(\alpha h \nu)^2$ versus $h\nu$ [41]. The respective bandgap energies are estimated to be 2.49, 0.98 and 1.62 eV by extrapolation (dashed lines in Fig. 8a). This absorbance spectrum is fundamentally different than that of a pure single crystal, which shows a direct absorption with the bandgap of 2.40 eV [40], ascribed to the transition between valence and conduction bands. This observed behaviour of three absorption regions, which has not been reported before for this material, suggests that the other two bandgap energies around 1.67 and 0.98 eV belonged to the mid-trap state caused by –Cd dangling bond and $S^{+2}$ levels [42]. The bandgap energy at 2.49 eV was ascribed to the transition between valence and conduction bands. The absorbance spectrum of CdS was fundamentally similar to that of pure CdS nanoparticles. The absorbance spectrum of CdS with $Pb^{2+}$ is fundamentally similar to that of pure CdS nanoparticles, with absorption at 1.97 and 2.09 eV. These shifts of the absorption bands were caused by the added lead. The main band redshifts slightly; the second one is increased reaching a maximum at $x = 13.61$ and then decreases slightly; the third one is blueshifted and then disappears for the same lead molar fraction. The slight reduction of the main absorption edge is indicative of the compensation of broken bonds, but also it indicates that the lead atoms are being incorporated into interstitials of the unit cell (see Table 2). The optical bandgap energy of the CdS nanofilm is 2.49 eV that corresponds to pure CdS and is 91 meV higher
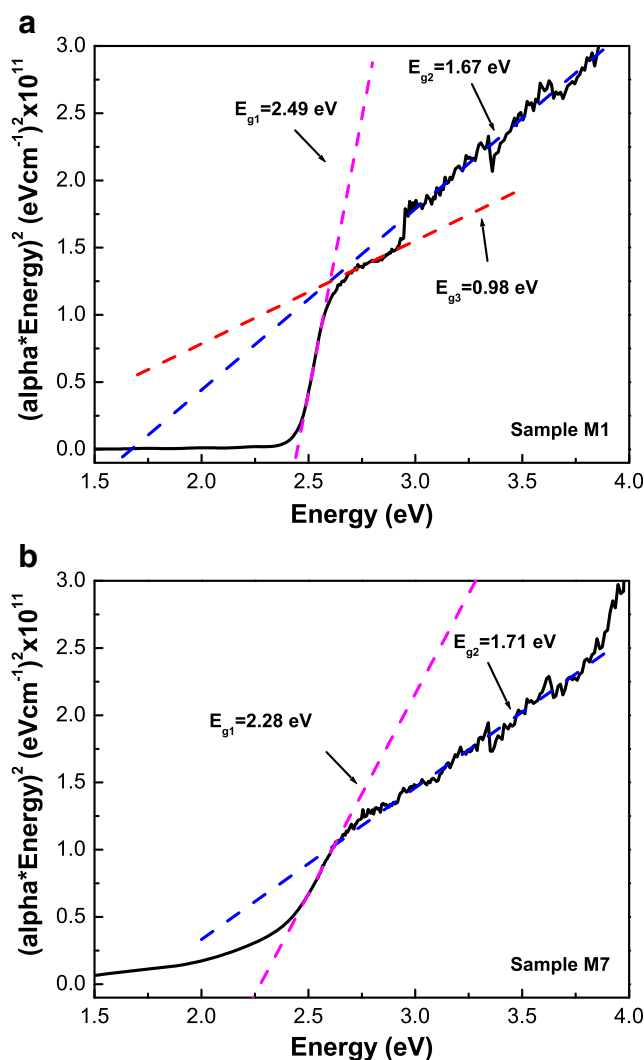


Fig. 8 Tauc plots: **a** CdS and **b** CdS with addition of $V[Pb^{2+}]\sim19.67\%$

than the bandgap in CdS bulk. This discrepancy is associated to the average grain size [38, 39]. In order to the M7 sample the optical bandgap energy decreased slightly by about 228 meV compared with the bandgap energy of the M1 sample, which can be related to $Pb^{2+}$ incorporation to the molecule and the average grain size, as can be seen in Fig. 8. This bandgap energy decrease can be explained by the substitution in the lattice of cadmium atoms (ionic radii ~0.97 Å) by lead atoms that are higher (ionic radii ~1.20 Å).

## 4 Conclusions

This work present the growth and characterization of ternary CdS:$Pb^{2+}$ nanofilms obtained by chemical bath deposition technique by under our proposed reactant species and at $20 \pm 2$ °C as deposited temperature. The results of the studies of X-ray diffraction and Raman spectroscopy show that grown CdS:$Pb^{2+}$ nanofilms belong to the zincblende crystalline

systems. The mean grain sizes of the nanocrystals are in the range of 1.21–6.67 nm, which were determined using the Debye–Scherrer equation for the ZB(111) direction and that were confirmed by HRTEM, although with this technique were obtained larger sizes. This mean grain size indicates a high quantum confinement. Raman scattering show that the lattice dynamics is characteristic of bimodal behaviour and the multipeaks adjust of the first optical longitudinal mode for the CdS:Pb denotes in all cases the Raman frequency of the characteristic peak is in the range of 305–298 cm$^{-1}$ of the CdS nanocrystals associated with the lead. CdS:Pb system presents three bandgaps that can be varied by Pb molar fractions incorporated in the nanolayers, which were obtained by transmittance measurements at room temperature. The main absorption band is observed at higher energies than the bandgap energy of bulk CdS; therefore, it is associated with the quantum confinement due to grain size, and it is redshifted slightly around 220 meV with increasing the molar fraction of lead over the range investigated. The other two absorption bands are associated with vacancies and interstices of cadmium and sulphur; one increases and another disappears as V[Pb$^{2+}$] is increased.

# References

1. Jeff, Hecht, Understanding Lasers, 2nd ed., IEEE Press, New York NY(USA), 1994.
2. Q. Q. Liu, J. H. Shi, Z. Q. Li, D. W. Zhang, X. D. Li, Z. Sun, L. Y. Zhang, S. M. Huang, Physica B **405**, 4360 (2010)
3. J.I. Contreras-Rascón, J. Díaz-Reyes, J. E. Flores-Mena, M. Galván-Arellano, L. A. Juárez-Morán, R. S. Castillo-Ojeda. Curr. Appl. Phys. 15 (2015) 1568
4. H. M. Upadhyaya, S. Chandra. J. Mater. Sci. 29 (1994) 2734.
5. J. Díaz-Reyes, E. López-Cruz, J. G. Mendoza-Álvarez, S. Jiménez-Sandoval, J. Appl. Phys. **100**, 123503 (2006)
6. S. Radhu, C. Vijayan, Mater. Chem. Phys. **129**, 1132 (2011)
7. W. Q. Peng, G. W. Cong, S. C. Qu, Z. G. Wang, Nanotechnology **16**, 1469 (2005)
8. J. Singh, in *Physics of Semiconductors and Their Heterostructures*, ed by McGraw-Hill. (1993)
9. K. Yamaguchi, T. T. Yoshida, M. S. Hideki, J. Phys. Chem. B **102**, 9677 (1998)
10. A. Abdulahzadeh Ziabari, F. E. Ghodsi. J. Lumin. 141 (2013) 121.
11. G. Murugadoss. Superlattice. Microst. 52 (2012) 1026.
12. M. Guglielmi, A. Martucci, J. Fick, G. Vitrant, J. Sol-Gel Sci. Technol. **11**, 229 (1998)
13. J. A. Lange's, *Handbook of Chemistry* (McGraw Hill Book Co., Beijing, 1999)
14. J. A. Dean, Lange's. Handbook of Chemistry, 13th ed. (New York: McGraw-Hill. 1987).
15. R. Ortega-Borges, D. Lincot, J. Electrochem. Soc. **140**, 3464 (1993)
16. M. Grus, A. Sikorska, Phys. B Condens. Matter **266**, 139 (1999)
17. J. Díaz-Reyes, J. I. Contreras-Rascón, J. S. Arias-Cerón, J. F. Sánchez-Ramírez, M. Galván-Arellano, J. Martínez-Juárez, J. A. Balderas-López, Mat. Sci. Semicon. Proc 37, 199 (2015)
18. M. Esmaili, A. Habibi-Yangjeh, Chin. J. Catal. **32**, 933 (2011)
19. M. R. Langille, M. L. Personick, J. Zhang, C. A. Mirkin, J. Am. Chem. Soc. **134**, 14542 (2012)
20. M. Grzelczak, J. Pérez-Juste, P. Mulvaney, L. M. Liz-Marzán, Chem. Soc. Rev. **37**, 1783 (2008)
21. P. Nandakumar, C. Vijayan, M. Rajalakshmi, A. K. Arora, Y. V. G. S. Murti, Phys. E. **11**, 377 (2001)
22. G. A. de Wijs, R. A. de Groot, Electrochim. Acta **46**, 1989 (2001)
23. A. Rougier, F. Portemer, A. Quédé, M. El Marssi, Appl. Surf. Sci. **153**, 1 (1999)
24. M. Regragui, M. Addou, A. Outzourhit, J. C. Bernéde, E. Elb El Idrissi, A. Benseddik, Kachouane. Thin Solid Films **358**, 40 (2000)
25. G. D. Smith, S. Firth, R. J. H. Clark, M. Cardona, J. Appl. Phys. **92**, 4375 (2002)
26. E. J. Donahue, A. Roxburgh, M. Yurchenko, Mater. Res. Bull. **33**, 323 (1998)
27. C. A. Argüello, D. L. Rousseau, S. P. S. Porto, Phys. Rev. **181**, 1351 (1969)
28. M. Abdulkhadar, B. Thomas, Nanostruct. Mater. **5**, 289 (1995)
29. M. Froment, M. Claude-Bernard, R. Cortes, B. Mokili, D. Lincot. J. Electrochem. Soc. **142**, 2642 (1995)
30. K. K. Nanda, S. N. Sarangi, S. N. Sahu, S. K. Deb, S. N. Behera, Phys. B Condens. Matter **262**, 31 (1999)
31. H. Brunner, H. Sussner, Biochim. Biophys. Acta **271**, 16 (1972)
32. V. Sivasubramanian, A. K. Arora, M. Premila, C. S. Sundar, V. S. Sastry, Physica E: Low-dimensional Systems and Nanostructures **31**, 93 (2006)
33. S. Kar, B. Satpati, P. V. Satyam, S. Chaudhuri, J. Phys. Chem. B **109**, 19134 (2005)
34. V. M. Dzhagan, I. Lokteva, M. Ya, Valakh, O. E. Raevska, J. Kolny-Olesiak, D. R. T. Zahn, J. Appl. Phys. **106**, 084318 (2009)
35. F. Comas, G. E. Nelson Studart, Marques. Solid State Commun. **130**, 477 (2004)
36. H. Lange, M. Artemyev, U. Woggon, C. Thomsen, Nanotechnology **20**, 045101 (2009)
37. M. R. Loghman-Estarki, M. Hajizadeh-Oghaz, H. Edris, R. S. Razavi, CrystEngComm **15**, 5898 (2013)
38. D. J. Seo, J. Korean Phys. Soc **45**, 1575 (2004)
39. B. J. Jin, H. S. Woo, S. Im, S. H. Bae, S. Y. Lee, Appl. Surf. Sci. **169/170**, 521 (2001)
40. A. I. Oliva, O. Solís-Canto, R. Castro-Rodríguez, P. Quintana, Thin Solid Films **391**, 28 (2001)
41. J. L. Pankove, *Optical Processes in Semiconductors* (Prentice-Hall, Englewood Cliffs, NJ), p. 1971
42. F. Gao, Y. Wang, L. Zhang, W. Yang, L. An, J. Am. Ceram. Soc. **93**, 1364 (2010)